Dalton Transactions

ROYAL SOCIETY OF CHEMISTRY

PAPER

View Article Online
View Journal | View Issue

Cite this: *Dalton Trans.*, 2025, **54**, 14001

Formation of a Mn^{III}–O–Ce^{IV} species from a Mn^{III}-hydroxo complex and ceric ammonium nitrate

Anagha Puthiyadath, Patrick Murphy, Delara Mafi, Purti Patel and Timothy A. Jackson *

Received 22nd July 2025,
Accepted 26th August 2025

DOI: 10.1039/d5dt01728a

rsc.li/dalton

The addition of 1.0 equiv. ceric ammonium nitrate (CAN) to the Mn^{III}-hydroxo complex $[Mn^{III}(OH)(PaPy_2Q)]^+$ (**1**) yields a new species (**2**) that contains a Mn^{III}–O–Ce^{IV} core. The Mn^{III} oxidation state in **2** is supported by ^{1}H NMR data, which reveal hyperfine-shifted protons from the $PaPy_2Q$ ligand, and a solution magnetic moment of 4.87μ_B, consistent with an S = 2 Mn^{III} ion. Analysis of Mn K-edge EXAFS data for **2** shows a Ce ion 3.8 Å from the Mn center, supportive of the Mn^{III}–O–Ce^{IV} core. Complex **2** reacts with excess ferrocene to generate only 1.0 equiv. of the ferrocenium ion. Because **1** is unreactive with ferrocene, we attribute this stoichiometry to the presence of one Ce^{IV} ion in **2**. Complex **2** can oxidize PPh_3 and tri-*tert*-butylphenol, with enhanced reactivity relative to **1**. We find no evidence that CAN oxidizes the Mn^{III} center in **1**, even when using excess CAN at low temperatures. This result stands in contrast to the reactivity of similar systems, where excess CAN converted a Mn^{III}-hydroxo complex to a complex with a Mn^{IV}–O–Ce^{IV} core (Karmalkar *et al. Angew. Chem., Int. Ed.*, 2019, **58**, 16124–16129). We discuss the basis for these different reactivities.

Introduction

Ceric ammonium nitrate (CAN) is a strong oxidant commonly used in catalytic and stoichiometric processes that require the conversion of low- or mid-valent transition metals to high-valent complexes.[1] For example, CAN is used as an oxidant in transition-metal-catalyzed water oxidation.[2–8] The strong oxidizing power of CAN is associated with the high reduction potential of the Ce^{IV}/Ce^{III} couple (1.37 V *vs.* SCE for $Ce(NO_3)_3$ in 1 M HNO_3).[9,10] However, the use of CAN introduces both a potent one-electron oxidant and strong Lewis acids (both Ce^{IV} and, potentially, its one-electron reduced product Ce^{III}). Consequently, oxidation of metal complexes by CAN often, but not always, generates metal–oxygen–cerium adducts.[11,12] For example, the oxidation of the *cis*-α isomer of $[Fe^{II}(OTf)_2(mcp)]$ (mcp = *N*,*N*′-dimethyl-*N*,*N*′-bis(2-pyridylmethyl)-1,2-*cis*-diaminocyclohexane) with >3 equiv. CAN yields a product with a O=Fe^{IV}–O–Ce^{IV} core (Fig. 1a).[13] On the other hand, oxidation of the *cis*-β isomer of $[Fe^{II}(OTf)_2(mcp)]$ with >3 equiv. CAN yields only the terminal iron(IV)-oxo complex lacking any interaction with Ce^{IV} or Ce^{III} ions (Fig. 1b).[13]

The reactions of Mn complexes with CAN have likewise revealed an impressive array of products, which exemplify the difficulty of correlating the identity of the product formed to specific features of the supporting ligand and/or reaction conditions. In several cases, the reaction of excess CAN (4.0 equiv.) with Mn^{II} complexes of pentadentate and tetradentate aminopyridyl ligands in 9 : 1 MeCN : H_2O yielded Mn^{IV}-oxo complexes.[14,15] The reason for using excess CAN in these reactions is uncertain, although the higher CAN concentration could increase the rates of Mn oxidation, limiting the possibility of side reactions. Our lab reported that the oxidation of a Mn^{II} complex of a pentadentate ligand by CAN in 9 : 1 MeCN : H_2O gives a variety of intermediates, including Mn^{IV}-oxo, bis(μ-oxo)dimanganese(III,IV), and bis(μ-oxo)dimanganese(IV,IV)

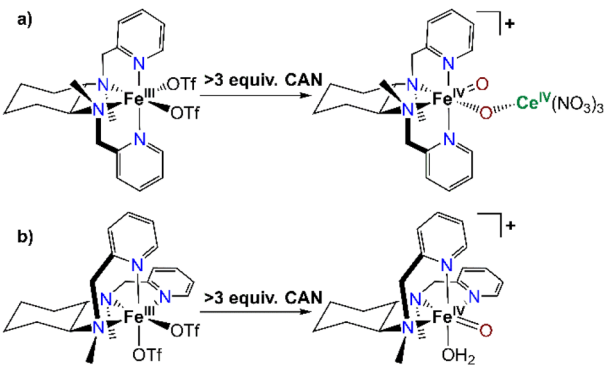

Fig. 1 Reactions of *cis*-α-$[Fe^{II}(OTf)_2(mcp)]$ (a) and *cis*-β-$[Fe^{II}(OTf)_2(mcp)]$ (b) with excess CAN.

The University of Kansas, Department of Chemistry and Center for Environmentally Beneficial Catalysis, 1567 Irving Hill Road, Lawrence, KS 66045, USA. E-mail: taj@ku.edu; Tel: +1 (785) 864-3968

species.[16] The Mn^{IV}-oxo intermediate accumulated initially, albeit in low yields (<40%), which we proposed allowed this complex to be trapped by a Mn^{III} complex to give the bis(μ-oxo) dimanganese(III,IV) intermediate. The bis(μ-oxo)dimanganese (III,IV) species was the final product for reactions with 1.5 equiv. CAN. For reactions with 2.0 equiv. CAN, the bis(μ-oxo)dimanganese(III,IV) species was further oxidized to give the bis(μ-oxo)dimanganese(IV,IV) complex as the final product.

In a separate case, the reaction of a Mn^{IV}-oxo complex, or its Mn^{IV}-hydroxo analogue, with $Ce^{III}(NO_3)_3$ yielded a product with a Mn^{III}–O–Ce^{IV} core (Fig. 2a).[17] This interesting reactivity demonstrates that Mn^{IV} centers can serve as oxidants to generate Ce^{IV} in some cases, suggesting similar $Mn^{IV/III}$ and $Ce^{IV/III}$ reduction potentials for certain manganese complexes. Alternatively, treatment of a Mn^{III}-hydroxo complex supported by the pentadentate, amide-containing ligand dpaq with 2 equiv. CAN yielded a product with a Mn^{IV}–O–Ce^{IV} core (Fig. 2b).[18] Thus, in this case, Ce^{IV} acts as both a one-electron oxidant, converting Mn^{III} to Mn^{IV}, and as a Lewis acid.

Most recently, Gupta and co-workers described that the addition of 4 equiv. CAN to a Mn^{II} complex supported by a tripodal TPA ligand (TPA = tris(pyridyl-2-methyl)amine) yielded a complex featuring a O=Mn^{IV}–O–Ce^{IV} motif (Fig. 2c).[19] The presence of the Mn^{IV}–O–Ce^{IV} unit was established from an analysis of EXAFS data, which revealed a Ce scatterer at 3.4 Å. Resonance Raman studies of this complex showed two bands sensitive to $^{16}O/^{18}O$ substitution, and one of these bands was in the range expected for a Mn=O vibration (710 cm^{-1}). In addition, the Mn K-edge pre-edge intensity of this complex was higher than that observed for related complexes with only the Mn–O–Ce motif, further implying the presence of the terminal Mn=O unit.

This diversity of products from reactions of Fe and Mn complexes with CAN raises an intriguing question. What factors control whether the reaction yields a metal–oxygen–cerium adduct, a terminal metal-oxo species, or an entirely different product? An answer to this question could guide the use of CAN as an oxidant for transition-metal complexes.

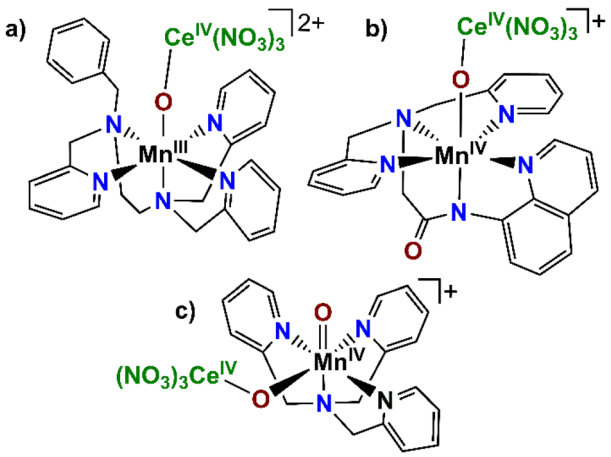

Fig. 2 Structures of Mn–O–Ce adducts from ref. 17 (a), 18 (b), and 19 (c). Although we show the Ce^{IV} ions associated with three nitrate ligands, the coordination of Ce^{IV} in these complexes is uncertain.

In this present work, we explore the reaction of CAN with the mononuclear Mn^{III}-hydroxo complex [Mn^{III}(OH)($PaPy_2Q$)] (OTf) (**1**; $PaPy_2Q$ = *N*-(2-aminoethyl)-2-quinoline-carboxamide, *N*,*N*-bis(2-pyridylmethyl)amine-*N*-ethyl-2-quinolinecarboxamide). Complex **1** has been well-characterized both structurally and spectroscopically in previous reports.[20,21] We find here that treatment of **1** with excess CAN does not result in oxidation of the Mn^{III} center. Instead, Ce^{IV} acts as a Lewis acid and converts the Mn^{III}–OH complex to a Mn^{III}–O–Ce^{IV} species (**2**).

Experimental methods

Materials and instrumentation

All chemicals and solvents used were of ACS reagent-grade or higher and were purchased from commercial suppliers. Unless otherwise specified, chemicals and solvents were used without further purification. Electronic absorption spectra were recorded using either an Agilent 8453 or a Varian Cary 50 Bio spectrophotometer, both integrated with a Unisoku cryostat (USP-203-A) for temperature regulation. ^{1}H NMR spectra were recorded using a Bruker DRX 400 MHz NMR spectrometer. For the hyperfine-shifted ^{1}H NMR spectra, a spectral window ranging from 150 to −100 ppm was used, with 1000 scans performed to ensure a high signal-to-noise ratio. Baseline correction was carried out using the multipoint fitting method with spline functions in the MestReNova software. EPR spectra were collected on a Bruker EMXPlus instrument with an ER4116DM dual-mode cavity. Temperature control was achieved using an Oxford Instruments ESR900 continuous-flow cryostat and ITC503 controller. All spectra were collected at X-band frequency and, unless otherwise noted, in perpendicular mode. Cyclic voltammograms were recorded at room temperature using an Epsilon potentiostat (BAS). The working electrode was a glassy carbon electrode with a Pt wire as the counter electrode. A Ag/AgCl quasi-reference electrode was used and $Fc^{+/0}$ potential was measured as an external reference. Before each experiment, the working electrode was thoroughly polished, then rinsed with deionized water and ethanol.

Synthesis and characterization

Synthesis of $PaPy_2QH$, [Mn^{II}($PaPy_2Q$)](OTf)·CH_3CN, and [Mn^{III}(OH)($PaPy_2Q$)](OTf) (**1**) were done based on methods previously reported in the literature.[20,21] Complex **2** was synthesized by adding 1 equiv. CAN (1.4 mg, 100 μL) to 2.0 mL of a 1.25 mM solution of **1**. The formation of the μ-oxomanganese(III)cerium(IV) product **2** was monitored by electronic absorption spectroscopy.

EPR and XAS sample preparation

EPR and XAS samples of **2** were prepared by reacting **1** with 1 equiv. CAN. In this procedure, 4 mg (0.006 mmol) of **1** were dissolved in 1 mL of MeCN and transferred to a quartz cuvette with a 0.2 cm pathlength. After the solution cooled to 0 °C, 3.3 mg (0.006 mmol) of CAN in MeCN were added. The reaction was monitored using electronic absorption spectroscopy. Once the intermediate **2** reached its maximum absorption,

approximately 250 μL of the solution were transferred into a 4 mm quartz EPR tube or an XAS cup and flash-frozen in liquid nitrogen. Experimental conditions for EPR data collection are provided in the relevant figure caption. Details on XAS data collection are discussed in the following section.

Mn K-edge X-ray absorption spectroscopy

Mn K-edge X-ray Absorption Spectroscopy (XAS) data were collected at beamline 7–3 of the Stanford Synchrotron Radiation Lightsource (SSRL) using a Si(220) monochromator and a 30-element Ge solid-state detector (Canberra). The measurements were taken using fluorescence excitation over an energy range of 6310 eV to 7300 eV at 15 K. To check for any photoreduction, the edge position was carefully monitored, but no such reduction was observed. A reference spectrum from manganese foil was recorded at the same time for internal calibration, with the edge energy set to 6539.0 eV, determined from the spectrum's inflection point. The data were processed and analyzed using the DEMETER software package. After processing, all data sets were merged, and the post-edge region was used for normalization. To analyze the Extended X-ray Absorption Fine Structure (EXAFS), FEFF6 was used to calculate phase and amplitude based on models generated from DFT-optimized structures.

Electronic structure computations

All electronic structure calculations were performed using *ORCA* 6.0.1.[22–25] All calculations were performed at the spin unrestricted level. Calculations for models of **1** and **2** were converged to the $S = 2$ spin state. These calculations employed the TPSS functional,[26] with ZORA–def2–SVP basis sets for C and H atoms and larger ZORA–def2–TZVP basis sets for Mn, O, and N.[27] The SARC–ZORA–TZVP basis set was used for Ce.[28] The zero-order-regular approximation (ZORA) was used to treat relativistic effects, and dispersion effects were accounted for using the Becke–Johnson damping scheme (D3 keyword[29,30] in *ORCA*). The resolution of the identity (RI) approximation[31] was used, and auxiliary basis sets were called using the AutoAux keyword.[32] We evaluated the efficacy of this method in treating the metric parameters of a Ce complex by calculating the structure of the hexa(nitrate)cerium(IV) anion. Our DFT structure has Ce–O, O–N (bound oxygen), and O–N (unbound oxygen) distances of 2.545, 1.280, and 1.231 Å, respectively, which accord well with reported crystallographic distances of 2.508, 1.282, and 1.234 Å.[33] On this basis, we concluded that this level of theory is reasonable for determining structures of Ce complexes for the purposes of this study. All reported MO compositions are for Kohn–Sham orbitals, and surface contour plots are of quasi-restricted orbitals (QROs). Cartesian coordinates for all DFT structures are in the SI (Tables S1–S3).

Results and analysis

Reaction of $[Mn^{III}(OH)(PaPy_2Q)]^+$ (1) with CAN to give 2

The Mn^{III}-hydroxo complex **1** (Scheme 1, top-left) has been previously characterized both structurally, by X-ray crystallography,[21] and spectroscopically, by electronic absorption and ^1H NMR methods.[20] The electronic absorption spectrum of **1** in

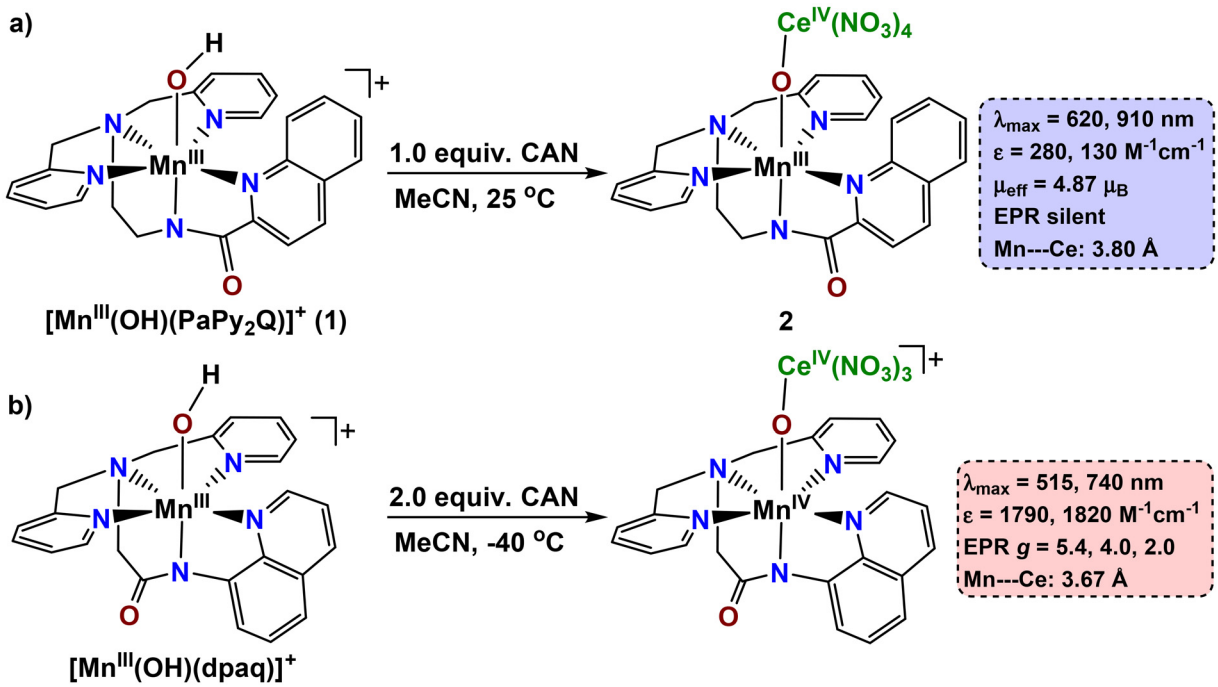

Scheme 1 Reactions of Mn^{III}-hydroxo complexes with CAN to give products with different spectroscopic properties. The top reaction (a) is the subject of this work; the bottom reaction (b) is described by Nam *et al.* in ref. 18.

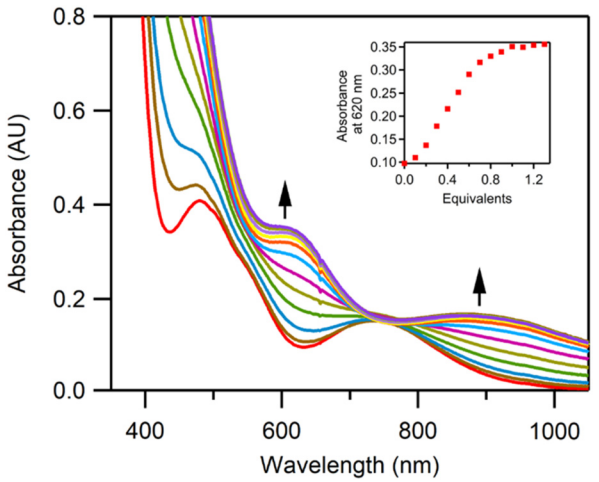

Fig. 3 Electronic absorption spectra showing the titration reaction of **1** with 0–1.4 equiv. CAN at 25 °C in MeCN. The red trace is the initial spectrum of **1** and the purple trace is the spectrum after the addition of 1.4 equiv. CAN. Intermediate spectra were taken after the addition of CAN in 0.1 equiv. increments.

MeCN displays bands at 485 and 734 nm (Fig. 3, red trace). The addition of CAN to **1** at 25 °C in MeCN results in the formation of **2**, with bands at 620 and 910 nm (Fig. 3) and only minor changes in the UV region (350–200 nm; see Fig. S1). This reaction is completed within two minutes (Fig. S1). The lack of large spectral changes in the UV region would be consistent with no change in the oxidation state of the supporting ligand. A titration of **1** with CAN shows that the formation of **2** maximizes after the addition of 1.0 equiv. CAN (Fig. 2, inset). Assuming a complete conversion of **1** to **2**, the 620 and 910 nm bands of **2** have extinction coefficients of 280 and 130 M^{-1} cm^{-1}. We observe the formation of **2** even when **1** is treated with 2.0 equiv. CAN at −40 °C (Fig. S1).

Although **1** and $[Mn^{III}(OH)(dpaq)]^+$ have very similar structures (Scheme 1, left), the reaction of **1** with CAN has several distinguishing features when compared to that of $[Mn^{III}(OH)(dpaq)]^+$ with CAN.[18] The reaction of $[Mn^{III}(OH)(dpaq)]^+$, performed at −40 °C, yielded a μ-oxomanganese(IV)cerium(IV) species (Fig. 2b) with electronic absorption bands at 515 and 740 nm. The absorption intensities for these bands were significantly greater than those of the starting Mn^{III}-hydroxo complex $[Mn^{III}(OH)(dpaq)]^+$. We reproduced this reaction following the reported procedures[18] and determined extinction coefficients for the μ-oxomanganese(IV)cerium(IV) complex of 1790 M^{-1} cm^{-1} and 1820 M^{-1} cm^{-1} for the 515 and 740 nm bands, respectively. In contrast, the extinction coefficients for the electronic absorption bands of $[Mn^{III}(OH)(dpaq)]^+$ at 550 and 780 nm are 320 and 130 M^{-1} cm^{-1}, respectively.[34] Moreover, a titration of $[Mn^{III}(OH)(dpaq)]^+$ showed maximum formation of the μ-oxomanganese(IV)cerium(IV) complex with 2.0 equiv. CAN. There was no evidence for an intermediate species formed when 1.0 equiv. CAN were added. These differences between the reactivity of $[Mn^{III}(OH)(dpaq)]^+$ and **1** with CAN are summarized in Scheme 1. Given the very similar structures of these Mn^{III}-hydroxo complexes, it is unexpected that these reactions should yield different products.

Characterization of 2

We performed a variety of spectroscopic experiments to gain insight into the nature of **2**. An Evans NMR experiment for **2** in MeCN yielded a magnetic moment of 4.87μ_B (Fig. S2), consistent with a high-spin Mn^{III} center and a closed shell Ce^{IV} center. The magnetic moment for **2** is only slightly perturbed compared to that reported for **1** (4.91μ_B).[20] The X-band, perpendicular-mode EPR spectrum of **2** at 10 K shows a weak, six-line signal centered at g = 2.0 (Fig. S3). Based on spin quantification, this signal accounts for only 4% of the Mn in the sample, indicating that the majority of Mn in **2** (96%) is EPR silent at X-band frequency. The room-temperature ^{1}H NMR spectrum of **2** is also consistent with a mononuclear Mn^{III} complex, showing several hyperfine-shifted proton resonances from ~60 to −20 ppm (Fig. 4). The ^{1}H NMR spectra do not show signals for (μ-oxo)dimanganese(III,III) complexes, which have been observed previously for similar systems.[35,36] The ^{1}H NMR spectrum of **2** shows some perturbations relative to that of **1** (*cf.* Fig. 4, top and bottom), which could reflect some changes in Mn–ligand bond lengths. Collectively, the solution magnetic moment, EPR data, and ^{1}H NMR data provide strong evidence that **2** contains a Mn^{III} center.

We further compared the geometric and electronic properties of **1** and **2** using Mn K-edge XAS data. Each complex shows a pre-edge peak near 6540 eV, with **2** showing a more intense peak and a more prominent pre-edge shoulder near 6542 eV (Fig. 5). Both complexes show a similar edge shape, with **2** having a higher-energy edge by 1.5 eV. We note that while an edge shift can be taken as evidence of a change in oxidation state, the edge energy is sensitive to a panoply of factors, and caution must be taken in inferring metal oxi-

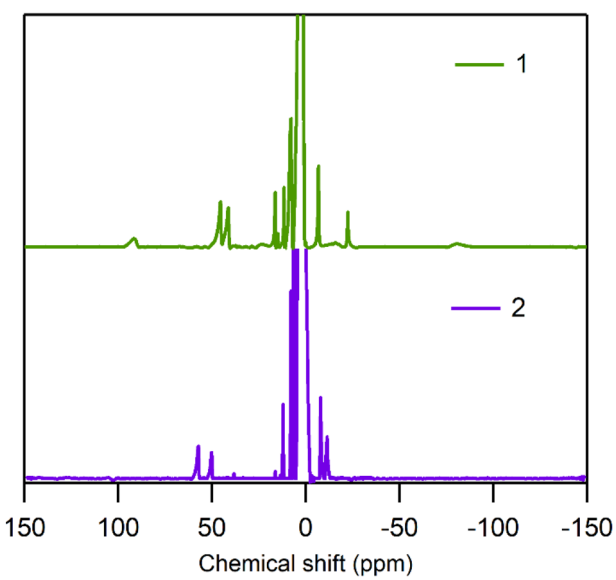

Fig. 4 ^{1}H NMR spectra of **1** and **2** in CD_3CN at 25 °C.

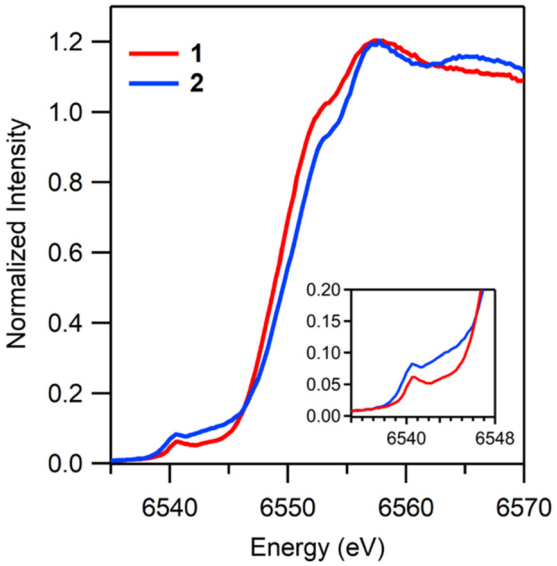

Fig. 5 Mn K-edge X-ray absorption near-edge spectra of **1** and **2**.

dation state from the edge energy alone.[37] The collective set of spectroscopic data for **2**, including the ^{1}H NMR data and magnetic moment, are consistent with a Mn^{III} assignment. Moreover, a more prominent edge shift was observed when the $[Mn^{III}(OH)(dpaq)]^+$ complex was treated with CAN to yield a Mn^{IV}–O–Ce^{IV} species, although a value for the edge shift was not reported.[18]

The Fourier transform (FT) EXAFS spectrum of **2** shows peaks at 1.3, 1.7, 2.1, 2.4, and 3.4 Å (Fig. 6, top). The peak at 3.4 Å is quite intense and indicates a heavy-atom scatterer at a relatively long distance from the Mn center. In support, the

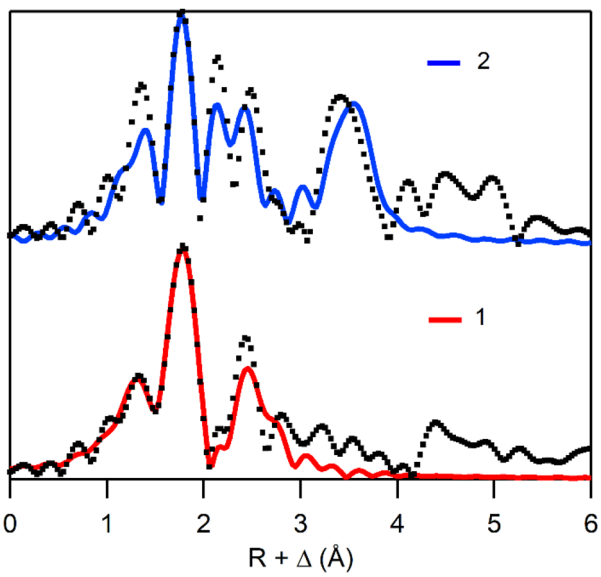

Fig. 6 Top: Fourier-transform EXAFS data for **2** (black squares) and fit 5 from Table S4 (blue trace). Bottom: Fourier-transform EXAFS data for **1** (black squares) and fit 4 from Table S5 (red trace).

EXAFS data were well fit with a Ce scatterer 3.80 Å from the Mn center (Fig. 6 and S4). The best fit (Table 1, and fit 5, Table S4) also includes one oxygen atom at 1.90 Å, two nitrogen atoms at 2.17 Å, and six carbon atoms at 2.93 Å. We note that the quality of the fit is not very sensitive to the number of atoms in the nitrogen and oxygen shells (Table S4). The Mn–O and Mn–Ce distances for **2** are essentially identical to those reported by Draksharapu and co-workers for a complex with a O=Mn^{IV}–O–Ce^{IV} motif (Fig. 2c), which were 1.80 and 3.73 Å, respectively (Table 1).[19] EXAFS data for the complex with a Mn^{IV}–O–Ce^{IV} core reported by Nam and co-workers (Fig. 2b) were fit with shorter Mn–O and Mn–Ce distances of 1.69 and 3.67 Å (Table 1).[18]

For comparison, we collected and analyzed EXAFS data for a sample of **1** in frozen MeCN. The FT EXAFS spectrum for **1** lacks the peak at 3.4 Å that is so prominent in the FT EXAFS spectrum of **2** (Fig. 6). The best fit for the EXAFS data for **1** includes a short Mn–O distance (1.84 Å; see Tables 1 and S5), in good agreement with the bond length in the X-ray crystal structure (1.8180(16) Å) of the perchlorate salt of **1**.[21] The first shell of **1** is completed in the EXAFS fit with one N atom at 1.98 Å and three at 2.19 Å. These distances nicely match the Mn–N(amide) bond length of 1.9680(18) Å and the average of the remaining Mn–N distances (2.186 Å) in the crystal structure of **1**.[21] The longest Mn-scatterers for **1** come from two C shells at 2.90 and 3.10 Å, with no requirement for shells beyond these distances.

Reactivity of 2

Complex **2** reacts rapidly with 1.0 equiv. ferrocene in MeCN at 25 °C (Fig. S5, top). This reaction generates the ferrocenium cation in 0.95 equiv. relative to **2**. Separate experiments demonstrated that the Mn^{III}-hydroxo complex **1** does not react with ferrocene under identical conditions. We therefore attribute the reaction of **2** with ferrocene to the reduction of the Ce^{IV} ion in the Mn^{III}–O–Ce^{IV} unit. A ^{1}H NMR spectrum collected immediately following the reaction of **2** and 1.0 equiv. ferrocene shows several hyperfine-shifted peaks (Fig. S5, center), suggesting the Mn^{III} ion has not been reduced. EPR data collected after the reaction of **2** with ferrocene reveal weak Mn^{II} signals that account for only ~5% of the Mn in the sample (Fig. S5, bottom). Therefore, we conclude that the majority of Mn exists in an EPR-silent form, indicating that no reduction of the Mn^{III} center has occurred.

Adding excess PPh_3 to **2** in MeCN causes the optical signals of **2** to decay over 120 seconds (Fig. 7). This reaction yields a light brown solution with poorly resolved electronic absorption bands near 740, 550, and 450 nm. An analysis of the products by ESI-MS experiments reveals prominent signals due to $[HOPPh_3]^+$, **1**, and $[Mn^{II}(PaPy_2Q)]^+$ (Fig. S6). The ^{31}P NMR spectrum of the product solution also shows the formation of $OPPh_3$ (Fig. S7, top), and signal integration reveals that $OPPh_3$ forms in 75% yield relative to **2**. Because $OPPh_3$ is formally a two-electron oxidation product of PPh_3, the yield suggests that both Ce^{IV} and Mn^{III} are reduced by one electron in this reaction. In support, a ^{1}H NMR spectrum collected after this reac-

Table 1 Comparison of EXAFS fitting results for **2**, **1**, and previously reported Mn–O–Ce complexes[a]

	Mn–O			Mn–N			Mn···C			Mn···Ce		
Complex	*n*	*r*	σ^2	*n*	*r*	σ^2	*n*	*r*	σ^2	*n*	*r*	σ^2
2	1	1.90	2.5	2	2.17	3.0	6	2.93	8.3	1	3.80	2.4
1	1	1.84	1.8	1	1.98	2.1	4	2.90	4.6			
				2	2.19	4.0	2	3.10	3.1			
$[(dpaq)Mn^{IV}(\mu\text{-}O)Ce^{IV}(NO_3)_3]$[b]	1	1.69	5.6[c]	5	1.97	5.6[c]	9	2.93	8.9[c]	1	3.67	3.0
							2	3.18	8.9[c]			
$[(TPA)(O)Mn^{IV}(\mu\text{-}O)Ce^{IV}(NO_3)_3]^{+}$[d]	1	1.80	5.5	3	2.04	2.3	6	2.91	4.2	1[e]	3.73	2.7
				1	2.34	2.7						

[a] Distances (*r*) are given in Å and Debye–Waller factors (σ^2) are given as × 10^3 Å^2. [b] From ref. 18. [c] Indicates that σ^2 was fixed to be the same for scatterers in the same coordination shell (*i.e.*, O and N, and the two C shells). [d] From ref. 19. [e] This fit involved both single- and multiple-scattering pathways for Mn···Ce and Mn–O–Ce, respectively. The parameters shown are for the multiple-scattering pathway.

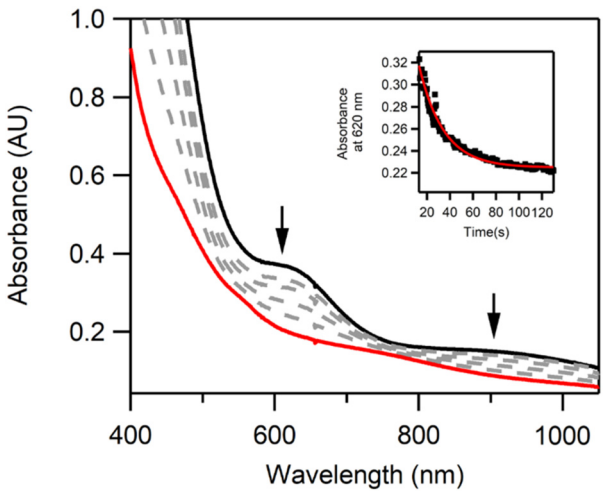

Fig. 7 Electronic absorption spectrum of **2** (black trace) upon the addition of 30 eq. PPh_3 in MeCN at 25 °C. The dashed traces show intermediate spectra, and the final spectrum is in red. The inset shows the decay of **2** over time (black circles) with a fit to a first-order decay (red trace).

tion does not show any hyperfine-shifted resonances, suggesting that the majority of the Mn^{III} ions have been reduced to Mn^{II} (Fig. S7, center). EPR spin quantification of the product reveals a six-line Mn^{II} signal near $g = 2$ that represents ~50% of the Mn in the sample (Fig. S7, bottom). The rate of decay of **2** upon the addition of excess PPh_3 can be fit to a first-order process to give a pseudo-first order rate constant, k_{obs} (Fig. 7, inset). The k_{obs} values increase with rising concentrations of PPh_3, and a linear fit to the k_{obs} *versus* $[PPh_3]$ yields a second-order rate constant (k_2) of 0.96 M^{-1} s^{-1} (Fig. S8). For comparison, the Mn^{III}-hydroxo complex **1** does not react with PPh_3. The previously reported $[(BnTPEN)Mn^{III}\text{-}O\text{-}Ce^{IV}(NO_3)_4]^{+}$ complex reacts more rapidly with PPh_3 than **2** (k_2 = 8.4 *vs.* 0.96 M^{-1} s^{-1}, both values at 25 °C in MeCN).[38] The difference in reactivity might arise from the negative charge of the $PaPy_2Q$ ligand compared to the neutral BnTPEN ligand, which could reduce the electrophilicity of the bridging oxo group.

To compare the reactivity of **2** with **1**, we explored the reaction of **2** with 2,4,6-tri-*tert*-butylphenol. Adding excess 2,4,6-tri-*tert*-butylphenol to **2** in MeCN at 50 °C led to the disappearance of the electronic absorption bands of **2** and the appearance of bands at 380, 400, and 628 nm (Fig. S9, top). These new bands are attributed to the formation of the 2,4,6-tri-*tert*-butylphenoxyl radical in >95% yield.[39] A control reaction of CAN with 2,4,6-tri-*tert*-butylphenol showed less than 5% formation of the 2,4,6-tri-*tert*-butylphenoxyl radical (Fig. S11). The ^{1}H NMR spectrum of the product formed from the reaction of **2** with 2,4,6-tri-*tert*-butylphenol is distinct from **1** and resembles the spectrum of the product formed when ferrocene was added to **2** (Fig. S10 and Table S6). A kinetic analysis of this reaction (Fig. S9, bottom) yields a second-order rate constant k_2 = 1.9 M^{-1} s^{-1} at 50 °C. This rate constant is 24-fold larger than that for the reaction of **1** with this substrate (k_2 = 0.08(1) M^{-1} s^{-1}).[20] Thus, replacement of the proton in **1** with the Ce^{IV} ion results in a marked increase in the rate of phenol oxidation.

Geometric and electronic structure of 2 from DFT computations

We used DFT computations to develop potential structures for **2**. The models considered differed only in the coordination environment of the Ce ion (all nitrate *versus* a mixture of nitrate and aqua ligands). All optimized models include a (μ-oxo)manganese–cerium core. The geometry around the Mn center changes very little in these models (Fig. 8 and Table 2), indicating that the exact environment of the Ce^{IV} ion does not have a marked effect on the structure of the Mn–O–Ce core or on the Mn–ligand bond lengths. In both models, the average Mn–N distances for the five donor nitrogens of the $PaPy_2Q$ ligand are near 2.15 Å, the Mn–O distance is ~1.80 Å, and the Mn–Ce separation is near 3.85 Å. A detailed comparison of the Mn–ligand distances in these models and that observed crystallographically for **1** is in the SI. The coordination geometry of the Ce^{IV} center in these models of **2** are very similar to those reported for CAN[33] and $[(N_4py)Fe^{III}\text{-}O\text{-}Ce^{IV}(OH_2)(NO_3)_4]^{+}$,[40] and this comparison is discussed in more detail in the SI. Overall, these DFT metric parameters are in excellent agreement with

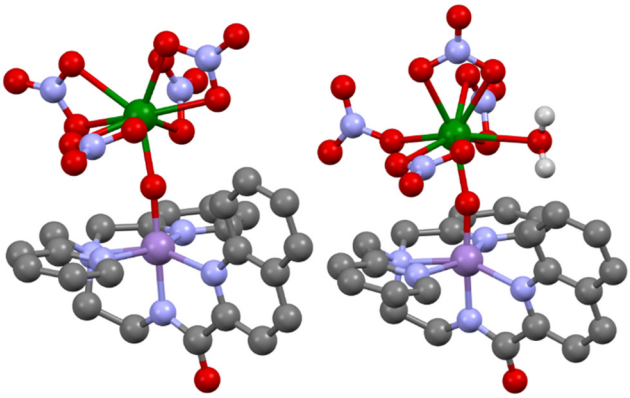

Fig. 8 Potential models of **2** from DFT computations.

those determined from the EXAFS data (Table 2), supporting our conclusion that **2** contains a (μ-oxo)manganese(III)–cerium(IV) core, with the Mn coordination geometry completed by the $PaPy_2Q$ ligand.

The Mn, O, and N spin densities from DFT calculations for **1** match closely those of the models of **2** (Table 2). A more detailed comparison of the bonding in **1** and **2** is provided by an analysis of the frontier MOs (Fig. 9). In this comparison we focus on [(PaPy$_2$Q)Mn-*O*-Ce(NO$_3$)$_4$] as the model for **2**. The Mn 3d MO splitting patterns of **1** and **2** are remarkably similar (see Fig. 9 and Tables S7 and S8). Each shows a Mn $(3d_{xy})^1(3d_{yz})^1(3d_{xz})^1(3d_{x^2-y^2})^1(3d_{z^2})^0$ configuration (using the coordinate system shown in Fig. 9, where the *z* axis lies along the Mn–OH bond and the *x* axis is along the Mn–N(quinoline) bond). The Mn $3d_{xy}$-based MO is at lowest energy, with the Mn $3d_{yz}$ and $3d_{xz}$ MOs ~1 to 1.5 eV higher in energy. The Mn $3d_{yz}$ and $3d_{xz}$ MOs are involved in π-interactions with the hydroxo (for **1**) and oxo (for **2**) ligands, as shown in the surface contour plots (Fig. 9). For both **1** and **2**, the Mn $3d_{x^2-y^2}$ MO is the spin-up (or α-spin) HOMO, with strong σ-antibonding interactions with the $PaPy_2Q$ ligand (Fig. 9). The Mn $3d_{z^2}$ MO is unoccupied and lies ~1.8 eV above the Mn $3d_{x^2-y^2}$ MO for both **1** and **2**. For complex **2**, the seven Ce 4f-based MOs are between the Mn $3d_{x^2-y^2}$ and Mn $3d_{z^2}$ MOs, making a Ce 4f MO the spin-up LUMO. This MO order has potential consequences for the reactivity of **2**, as it could imply that Ce^{IV} would be the site of reduction. Indeed, as described above, the reaction of **2** with ferrocene is marked by reduction of the Ce^{IV} center but not the Mn^{III} center.

An inspection of the MO compositions for **2** shows that there is only small mixing between the Ce and Mn orbitals. For example, the Mn $3d_{xz}$ and $3d_{yz}$ MOs carry the most Ce 4f character at ~4 to 7% (Table S7). This interaction is mediated by the π-orbitals of the oxo bridge. We also observe little mixing of Mn 3d character into the Ce 4f-based MOs. An exception is the Ce $4f_{z^3}$ MO that carries up to 7% Mn $3d_{z^2}$ character, mediated by a σ-orbital of the oxo bridge (Fig. S12).

Comparison of the electrochemical properties of 1 and $[Mn^{III}(OH)(dpaq)]^+$

Our collective spectroscopic data for **2** provides strong support for retention of the Mn^{III} oxidation state following the addition of CAN to the Mn^{III}-hydroxo complex **1**. In contrast, the $[Mn^{III}(OH)(dpaq)]^+$ complex, which has a structure very similar to that of **1**, is oxidized by CAN to generate a complex with a Mn^{IV}–O–Ce^{IV} core (Scheme 1).[18] We have previously noted that the peak potential ($E_{p,c}$) associated with reduction of the Mn^{III} center in **1** is more negative than that of $[Mn^{III}(OH)(dpaq)]^+$ (−0.86 V and −0.70 V *vs.* Fc^+/Fc, respectively).[20] Thus, despite their similarities, the $PaPy_2Q$ and dpaq ligands do show differ-

Table 2 Structural parameters for [Mn(OH)(PaPy$_2$Q)]ClO$_4$ (**1**) from X-ray crystallography[a] and potential structures for **2** from DFT computations

		2		
	1	[(PaPy$_2$Q)Mn-*O*-Ce(NO$_3$)$_4$]	[(PaPy$_2$Q)Mn-*O*-Ce(NO$_3$)$_4$(OH$_2$)]	EXAFS
Mn–N1	2.1945(19)	2.20	2.20	
Mn–N2	1.9680(18)	1.95	1.96	
Mn–N3	2.2415(19)	2.31	2.30	
Mn–N4	2.138(2)	2.16	2.18	
Mn–N5	2.171(2)	2.10	2.10	
Mn–N[b]	2.14	2.14	2.15	2.17
Mn–O1	1.8180(16)	1.80	1.79	1.90
Mn–Ce		3.85	3.84	3.80
O1–Ce		2.08	2.10	
Mn–O1–Ce		167.3	161.1	
Ce–O[b]		2.49	2.50	
			2.23	
			2.61	
Spin density (charge)				
Mn	3.86 (0.67)	3.83 (0.62)	3.80 (0.59)	
Ce		0.12 (1.54)	0.12 (1.54)	
O[c]	0.06 (−0.54)	0.01 (−0.71)	0.03 (−0.73)	
N[d]	−0.07 (−2.65)	−0.06 (−2.67)	−0.06 (−2.64)	

[a] **1** is [Mn(OH)(PaPy$_2$Q)]ClO$_4$ and structural data are from ref. 21. [b] Average bond lengths. [c] Spin density of the bridging oxo ligand (for **2**) or the hydroxo ligand (for **1**). [d] Total spin density of all nitrogen atoms of the $PaPy_2Q$ ligand.

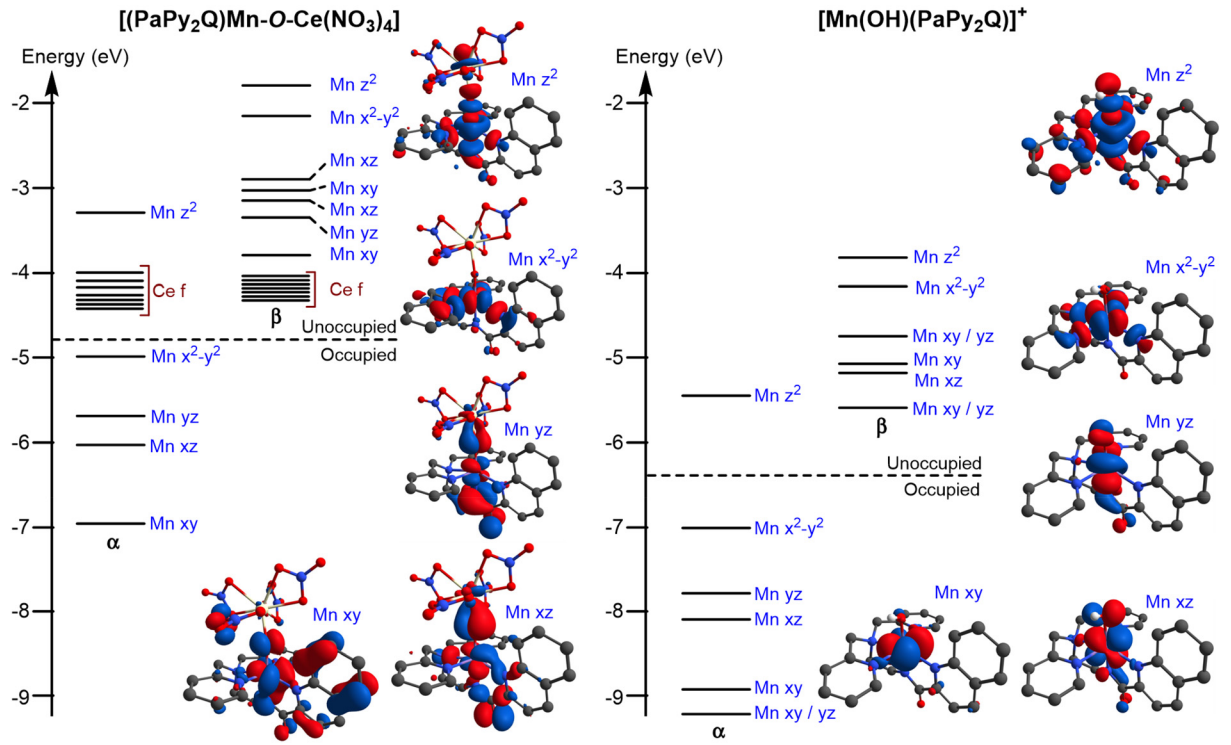

Fig. 9 Molecular orbital energy level diagrams of $[(PaPy_2Q)Mn\text{-}O\text{-}Ce(NO_3)_4]$ (left) and $[Mn^{III}(OH)(PaPy_2Q)]^+$ (right) from spin unrestricted TPSS-D3 ZORA DFT calculations.

ences in tuning metal redox potentials. In this section, we further explore the electrochemical properties of **1** and $[Mn^{III}(OH)(dpaq)]^+$ in order to investigate the basis for this difference in reactivity with CAN. For these experiments, we performed the electrochemical measurements in MeCN in the presence of 20 μL water. The water is required to ensure that the Mn^{III}-hydroxo species $[Mn^{III}(OH)(dpaq)]^+$ predominates in solution. We have shown that $[Mn^{III}(OH)(dpaq)]^+$ exists in equilibrium with $[Mn^{III}Mn^{III}(\mu\text{-}O)(dpaq)_2]^{2+}$, and added water shifts the equilibrium position in favor of the Mn^{III}-hydroxo complex.[35,36] Previously reported CV measurements for **1** were performed in MeCN without added water, as there is no evidence that this Mn^{III}-hydroxo complex equilibrates with a (μ-oxo)dimanganese(III,III) species.[20]

When **1** is swept to reducing potentials in a CV experiment, we observe a reduction wave at $E_{p,c} = -0.41$ V *vs.* Fc^+/Fc and a weak, corresponding oxidation wave at $E_{p,a} = -0.18$ V *vs.* Fc^+/Fc (Fig. 10, top; see Fig. S13 for scans from a differential pulse voltammetry experiment). We attribute these waves to the $Mn^{III/II}$ couple. Previously, we had reported an $E_{p,c}$ of −0.86 V for the reduction of **1**.[20] The less negative potential observed here is likely caused by the added water, which provides a source of protons. At higher potentials, we observed a reversible redox wave at $E_{1/2} = 0.5$ V *vs.* Fc^+/Fc ($\Delta E_p = 0.07$ V), which we assign to the $Mn^{IV/III}$ couple. Peaks at higher potentials ($E_{p,a} = 1.06$ and $E_{p,c} = 0.99$ V *vs.* Fc^+/Fc; $\Delta E_p = 0.07$ V) are also observed in a CV of the $HPaPy_2Q$ ligand (Fig. S13) and are therefore attributed to ligand-centered redox events.

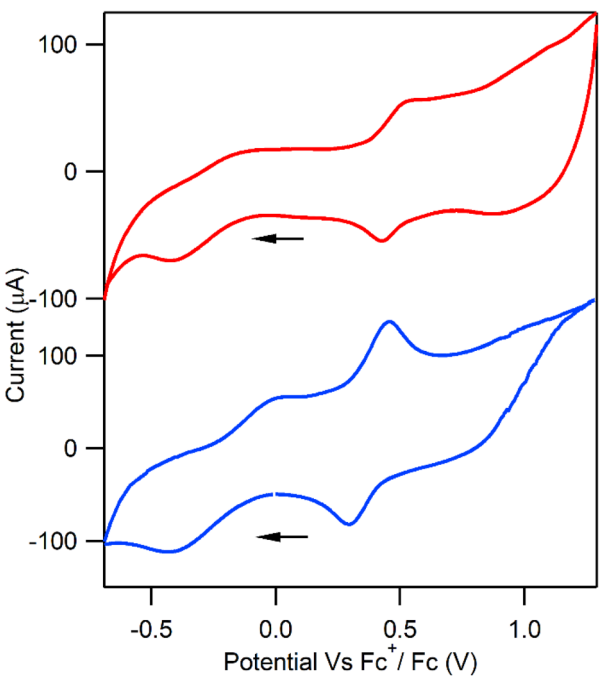

Fig. 10 Cyclic voltammograms of **1** (red, top) and $[Mn^{III}(OH)(dpaq)]^+$ (blue, bottom). Solutions are 2 mM in 5 mL MeCN with 20 μL H_2O, and 0.1 M $TBAPF_6$ as the supporting electrolyte. A 0.1 V s^{-1} scan rate was used in each case.

The corresponding CV of $[Mn^{III}(OH)(dpaq)]^+$ shows a set of redox couples similar to that of **1**. One set is observed at $E_{1/2}$ = −0.23 V *vs.* Fc^+/Fc (ΔE_p = 0.2 V) and is attributed to the $Mn^{III/II}$ couple. This potential compares well to that previously reported for $[Mn^{III}(OH)(dpaq)]^+$.[41] The $[Mn^{III}(OH)(dpaq)]^+$ complex also shows a reversible wave at 0.38 V *vs.* Fc^+/Fc, (ΔE_p = 0.09 V), which is assigned to $Mn^{IV/III}$ the couple. Thus, $[Mn^{III}(OH)(dpaq)]^+$ is oxidized at a lower potential than **1**. Although the potential of many Ce^{IV} complexes is higher than that of both Mn^{III}-hydroxo complexes, the Ce^{IV} potential is known to be quite sensitive to the Ce^{IV} coordination environment.[10,17] Indeed, Draksharapu and co-workers reported the ability of a Mn^{IV}-hydroxo complex to oxidize Ce^{III} to Ce^{IV} in MeCN.[17] Thus, we suggest that the difference in the $Mn^{IV/III}$ potential between **1** and $[Mn^{III}(OH)(dpaq)]^+$ can account for the different products formed upon reaction with CAN (Scheme 1).

Discussion

The past several years have seen increased interest in the oxidation products that are formed when CAN is used to oxidize Mn^{II} and Mn^{III} coordination complexes.[14–19,42] Such species are relevant to understanding the mechanisms by which transition-metal catalysts perform oxidation reactions using CAN as the terminal oxidant.[3,13] Although it is well known that changes to the Mn coordination sphere can lead to different products (see Fig. 1 and 2), it remains challenging to correlate the product formed to properties of the manganese complex. In this study, we explored the properties and reactivity of the product formed when the mononuclear Mn^{III}-hydroxo complex **1** reacts with CAN (**2**). On the basis of a variety of spectroscopic data, we conclude that **2** contains a Mn^{III}–O–Ce^{IV} core. Thus, we find no evidence that the addition of CAN to **1** results in oxidation of the Mn^{III} center but instead we observe a product where the proton of the Mn^{III}-hydroxo unit has been replaced with the Ce^{IV} Lewis acid (Scheme 1, top). This observed product contrasts with that previously reported for the related Mn^{III}-hydroxo complex $[Mn^{III}(OH)(dpaq)]^+$.[18] In that case the addition of CAN resulted in both oxidation of the Mn^{III} center to Mn^{IV} and the replacement of the proton with the Ce^{IV} Lewis acid (Scheme 1, bottom). We attribute this difference in product formed to the higher $Mn^{IV/III}$ reduction potential of **1** compared to $[Mn^{III}(OH)(dpaq)]^+$.

What causes this difference in potential for these structurally similar complexes? There are several examples where the donor properties of a pyridine or quinoline ligand are modulated by the addition of steric bulk adjacent to the metal center.[43–47] The steric bulk enforces longer metal–nitrogen bond lengths that in turn increase the metal ion reduction potential. For example, we have shown that a derivative of $[Mn^{III}(OH)(dpaq)]^+$ with a methyl-quinolyl group, where the methyl is pointed towards the Mn^{III}-hydroxo unit, has a $Mn^{III/II}$ peak potential ($E_{p,c}$) 0.09 V more positive than that of $[Mn^{III}(OH)(dpaq)]^+$.[43] An X-ray structure of the Mn^{III}-hydroxo complex with the methyl–quinolyl group showed a Mn–N(quinoline) bond 0.1 Å longer than that of $[Mn^{III}(OH)(dpaq)]^+$.[43] Similarly, the different orientation of the quinolyl group in **1** compared to $[Mn^{III}(OH)(dpaq)]^+$ places more steric bulk near the Mn center (Scheme 1, left). The Mn–N bond for **1** is 2.1945(19) Å,[21] notably longer than that of $[Mn^{III}(OH)(dpaq)]^+$ (2.072(14) Å).[34] On this basis, we conclude that subtle differences in Mn–N bond lengths cause the change in $Mn^{IV/III}$ potential.

DFT computations performed for **1** and models of **2** revealed that the replacement of the proton in **1** with the Ce^{IV} ion in **2** has only minor effects on the relative energies and compositions of the Mn 3d-based MOs (Fig. 9 and Tables S7 and S8). The main structural difference between these complexes is an elongation of the Mn–O bond in **2** (Table 2). An analysis of the frontier MOs (Fig. 9) shows that the Ce 4f orbitals interleave the Mn $3d_{x^2-y^2}$ spin-up HOMO and the Mn $3d_{z^2}$ spin-up LUMO, adding a manifold of new redox-active orbitals and making the Ce^{IV} center the preferred site of reduction.

This redox activity of the Ce^{IV} center in **2** opens access to new reaction channels unavailable to the Mn^{III}-hydroxo unit in **1**. While the Mn^{III}–OH unit in **1** acts exclusively as a one-electron oxidant, the Mn^{III}–O–Ce^{IV} unit in **2** can act as a two-electron oxidant. Specifically, **2** reacts with PPh_3 to give O=PPh_3 in ∼75% yield, while complex **1** is unreactive with PPh_3. The rate of PPh_3 oxidation by **2** is ∼9-fold less than that of a Mn^{III}–O–Ce^{IV} complex where the Mn^{III} center was supported by a neutral ligand (Fig. 2a).[17] While we postulate that the neutral ligand would increase the electrophilicy of the oxo bridge, future studies are needed to better explore the factors controlling the reactivity of Mn^{III}–O–Ce^{IV} complexes.

Our kinetic studies reveal that the Mn^{III}–O–Ce^{IV} core in **2** is significantly more reactive than the Mn^{III}–OH unit in **1**. For example, in reactions with 2,4,6-tri-*tert*-butylphenol, **2** shows a rate enhancement of 24-fold compared to **1**. Given that each of these reactions yields the tri-*tert*-butoxyl radical, we propose that phenol oxidation proceeds by a proton-coupled electron-transfer (PCET) mechanism. The ^{1}HNMR spectrum of the product formed after the reaction of **2** with 2,4,6-tri-*tert*-butylphenol shows that the Mn^{III}-hydroxo complex **1** is not a product. In fact, the ^{1}H NMR spectrum of the product resembles, but is distinct from, the product formed by ferrocene reduction of **2** (Fig. S10). We can rationalize the differences between the ^{1}H NMR spectrum of **1** and those of the reduced products by postulating the presence of a Mn–O(H)–Ce core when **2** is reduced (Scheme 2, bottom). The proximity of the paramagnetic Ce^{III} center to the $PaPy_2Q$ ligand would cause additional hyperfine shifts in the proton resonances relative to **2** and **1**.

For **1**, the electron acceptor is the Mn^{III} center and the proton acceptor is the hydroxo ligand, with the reaction yielding a Mn^{II}-aqua complex and tri-*tert*-butoxyl radical (Scheme 2, top).[20] In contrast, we propose that the Ce^{IV} center serves as the electron acceptor for **2**, with the bridging oxo ligand presumably acting as the proton acceptor (Scheme 2, bottom). In both cases, the reaction driving force is related to the bond dissociation free energy (BDFE) of the O–H bond formed in the

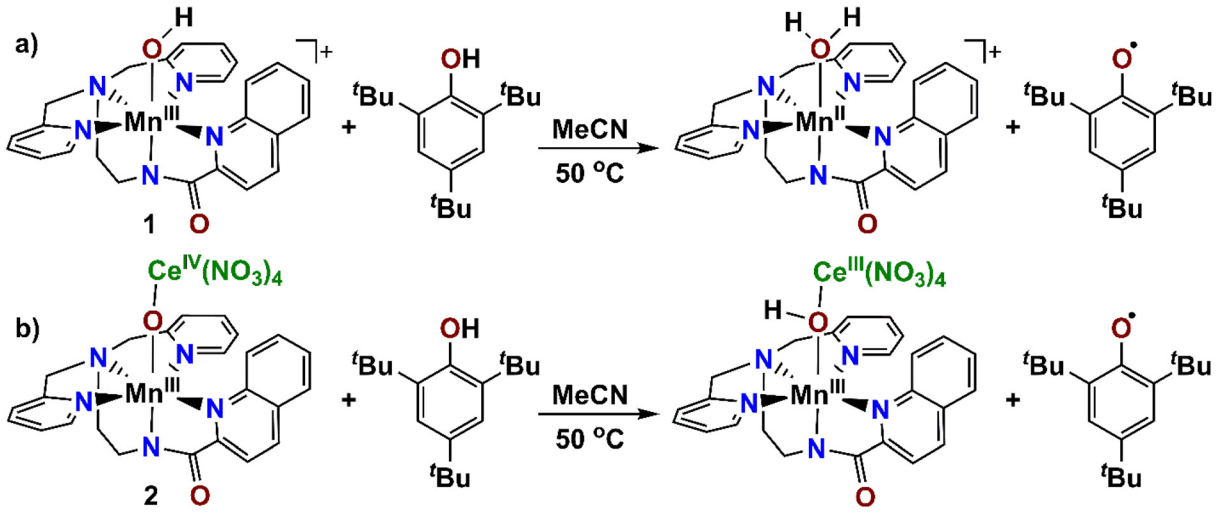

Scheme 2 Postulated reactions of **1** (a) and **2** (b) with tri-*tert*-butylphenol.

product. Using the Bordwell equation, this BDFE can be expressed in terms of the metal reduction potential and ligand (hydroxo or bridging oxo) pK_a (eqn (1)).

$$\mathrm{BDFE_{sol}(O{-}H)} = 1.37 \cdot \mathrm{p}K_a + 23.06 \cdot E^\circ + C_{\mathrm{G,sol}} \quad (1)$$

Thus, reactivity can be enhanced by either making the metal a better oxidant or making the ligand a stronger base. We presume that the enhanced reactivity of **2** compared to **1** is due to the Ce^{IV} center in **2** being a better electron acceptor than the Mn^{III} center in **1**. Future studies will further probe the basis for these differences in reactivity caused by the Ce^{IV} center.

Conclusions

In this work, we have examined the reactivity of CAN with the mononuclear Mn^{III}-hydroxo complex **1**. The addition of CAN to **1** causes marked changes in the UV-vis spectrum (Fig. 3), resulting in the formation of a new species, **2**. ^{1}H NMR and Evans NMR data provide strong evidence that **2** contains a Mn^{III} center. Mn K-edge XAS data and DFT computations for **2** provide support for the Mn^{III}–O–Ce^{IV} core. The presence of the Ce^{IV} species in **2** leads to enhanced and new reactivity compared to the Mn^{III}-hydroxo complex **1**. This work demonstrates the importance of considering a range of possible modes of interaction of Ce^{IV} with transition-metal complexes.

Conflicts of interest

The authors declare no conflicts of interest.

Data availability

The data supporting this article have been included as part of the SI: electronic absorption, NMR, and EPR data, EXAFS fits, kinetic plots, MO energies and compositions, and Cartesian coordinates from DFT computations. See DOI: https://doi.org/10.1039/d5dt01728a.

Acknowledgements

This work was supported by the U.S. National Science Foundation (CHE-2154955 to T. A. J.). The calculations were performed at the University of Kansas Center for Research Computing (CRC), including the BigJay Cluster resource funded through U.S. NSF Grant MRI-2117449. The use of the Stanford Synchrotron Radiation Lightsource, SLAC National Accelerator Laboratory, is supported by the U.S. Department of Energy, Office of Science, Office of Basic Energy Sciences under Contract No. DE-AC02-76SF00515. The SSRL Structural Molecular Biology Program is supported by the DOE Office of Biological and Environmental Research and by the National Institutes of Health and National Institute of General Medical Sciences (P30GM133894).

References

1 V. Nair and A. Deepthi, Cerium(IV) Ammonium NitrateA Versatile Single-Electron Oxidant, *Chem. Rev.*, 2007, **107**(5), 1862–1891, DOI: 10.1021/cr068408n.
2 J. L. Fillol, Z. Codolà, I. Garcia-Bosch, L. Gómez, J. J. Pla and M. Costas, Efficient water oxidation catalysts based on readily available iron coordination complexes, *Nat. Chem.*, 2011, **3**(10), 807–813, DOI: 10.1038/nchem.1140.
3 Z. Codolà, I. Garcia-Bosch, F. Acuña-Parés, I. Prat, J. M. Luis, M. Costas and J. Lloret-Fillol, Electronic Effects on Single-Site Iron Catalysts for Water Oxidation, *Chem. – Eur. J.*, 2013, **19**(25), 8042–8047, DOI: 10.1002/chem.201301112.

4 D. Hong, S. Mandal, Y. Yamada, Y.-M. Lee, W. Nam, A. Llobet and S. Fukuzumi, Water Oxidation Catalysis with Nonheme Iron Complexes under Acidic and Basic Conditions: Homogeneous or Heterogeneous?, *Inorg. Chem.*, 2013, **52**(16), 9522–9531, DOI: **10.1021/ic401180r**.

5 S. Fukuzumi, Y.-M. Lee and W. Nam, Kinetics and mechanisms of catalytic water oxidation, *Dalton Trans.*, 2019, **48**(3), 779–798, DOI: **10.1039/C8DT04341H**.

6 D. Moonshiram, I. Alperovich, J. J. Concepcion, T. J. Meyer and Y. Pushkar, Experimental demonstration of radicaloid character in a RuV=O intermediate in catalytic water oxidation, *Proc. Natl. Acad. Sci. U. S. A.*, 2013, **110**(10), 3765–3770, DOI: **10.1073/pnas.1222102110**.

7 W. C. Ellis, N. D. McDaniel, S. Bernhard and T. J. Collins, Fast Water Oxidation Using Iron, *J. Am. Chem. Soc.*, 2010, **132**(32), 10990–10991, DOI: **10.1021/ja104766z**.

8 D. B. Grotjahn, D. B. Brown, J. K. Martin, D. C. Marelius, M.-C. Abadjian, H. N. Tran, G. Kalyuzhny, K. S. Vecchio, Z. G. Specht, S. A. Cortes-Llamas, *et al.*, Evolution of Iridium-Based Molecular Catalysts during Water Oxidation with Ceric Ammonium Nitrate, *J. Am. Chem. Soc.*, 2011, **133**(47), 19024–19027, DOI: **10.1021/ja203095k**.

9 A. A. Noyes and C. S. Garner, Strong Oxidizing Agents in Nitric Acid Solution. I. Oxidation Potential of Cerous—Ceric Salts, *J. Am. Chem. Soc.*, 1936, **58**(7), 1265–1268, DOI: **10.1021/ja01298a051**.

10 N. A. Piro, J. R. Robinson, P. J. Walsh and E. J. Schelter, The electrochemical behavior of cerium(III/IV) complexes: Thermodynamics, kinetics and applications in synthesis, *Coord. Chem. Rev.*, 2014, **260**, 21–36, DOI: **10.1016/j.ccr.2013.08.034**.

11 R. Ezhov, A. K. Ravari and Y. Pushkar, Characterization of the FeV=O Complex in the Pathway of Water Oxidation, *Angew. Chem., Int. Ed.*, 2020, **59**(32), 13502–13505, DOI: **10.1002/anie.202003278**.

12 A. Draksharapu, S. Xu and L. Que Jr, Ce^{IV}- and, $HClO_4$-Promoted Assembly of an $Fe_2IV(\mu\text{-}O)_2$ Diamond Core from its Monomeric FeIV=O Precursor at Room Temperature, *Angew. Chem., Int. Ed.*, 2020, **59**(50), 22484–22488, DOI: **10.1002/anie.202010027**.

13 Z. Codolà, L. Gómez, S. T. Kleespies, L. Que Jr, M. Costas and J. Lloret-Fillol, Evidence for an oxygen evolving iron–oxo–cerium intermediate in iron-catalysed water oxidation, *Nat. Commun.*, 2015, **6**(1), 5865, DOI: **10.1038/ncomms6865**.

14 X. Wu, X. Yang, Y.-M. Lee, W. Nam and L. Sun, A nonheme manganese(IV)-oxo species generated in photocatalytic reaction using water as an oxygen source, *Chem. Commun.*, 2015, **51**(19), 4013–4016, DOI: **10.1039/c4cc10411k**.

15 P. Barman, A. K. Vardhaman, B. Martin, S. J. Wörner, C. V. Sastri and P. Comba, Influence of Ligand Architecture on Oxidation Reactions by High-Valent Nonheme Manganese Oxo Complexes Using Water as a Source of Oxygen, *Angew. Chem., Int. Ed.*, 2015, **54**(7), 2095–2099, DOI: **10.1002/anie.201409476**.

16 Y. Lee, A. Puthiyadath, S. D. Jones, M. C. Denler, P. Murphy, D. Mafi and T. A. Jackson, Ceric Ammonium Nitrate Oxidation of a MnII Complex Generates a Bis(μ-oxo) dimanganese(IV,IV) Product via a MnIV–Oxo Intermediate, *Inorg. Chem.*, 2024, **63**(46), 21919–21928, DOI: **10.1021/acs.inorgchem.4c03205**.

17 S. Gupta, P. Arora, R. Kumar, A. Awasthi, B. Chandra, R. Eerlapally, J. Xiong, Y. Guo, L. Que Jr and A. Draksharapu, Formation of a Reactive [Mn(III)–O–Ce(IV)] Species and its Facile Equilibrium with Related Mn(IV)(OX) (X = Sc or H) Complexes, *Angew. Chem., Int. Ed.*, 2024, **63**(3), e202316378, DOI: **10.1002/anie.202316378**.

18 D. G. Karmalkar, M. Sankaralingam, M. S. Seo, R. Ezhov, Y.-M. Lee, Y. N. Pushkar, W.-S. Kim, S. Fukuzumi and W. Nam, A High-Valent Manganese(IV)–Oxo–Cerium(IV) Complex and Its Enhanced Oxidizing Reactivity, *Angew. Chem., Int. Ed.*, 2019, **58**(45), 16124–16129, DOI: **10.1002/anie.201910032**.

19 S. Gupta, P. Arora, Z. Aghaei, B. Singh, T. A. Jackson and A. Draksharapu, Formation and Reactivity of a MnIV(O)(μ-O) CeIV Species: A Closest Mimic of Photosystem II, *J. Am. Chem. Soc.*, 2025, **147**(1), 619–626, DOI: **10.1021/jacs.4c12523**.

20 A. A. Opalade, L. Hessefort, V. W. Day and T. A. Jackson, Controlling the Reactivity of a Metal-Hydroxo Adduct with a Hydrogen Bond, *J. Am. Chem. Soc.*, 2021, **143**(37), 15159–15175, DOI: **10.1021/jacs.1c06199**.

21 A. A. Eroy-Reveles, Y. Leung, C. M. Beavers, M. M. Olmstead and P. K. Mascharak, Near-Infrared Light Activated Release of Nitric Oxide from Designed Photoactive Manganese Nitrosyls: Strategy, Design, and Potential as NO Donors, *J. Am. Chem. Soc.*, 2008, **130**(13), 4447–4458, DOI: **10.1021/ja710265j**.

22 F. Neese, The ORCA program system, *Wiley Interdiscip. Rev.: Comput. Mol. Sci.*, 2012, **2**(1), 73–78, DOI: **10.1002/wcms.81**.

23 F. Neese, Software update: the ORCA program system, version 4.0, *Wiley Interdiscip. Rev.: Comput. Mol. Sci.*, 2018, **8**(1), e1327, DOI: **10.1002/wcms.1327**.

24 F. Neese, Software update: The ORCA program system—Version 5.0, *Wiley Interdiscip. Rev.: Comput. Mol. Sci.*, 2022, **12**(5), e1606, DOI: **10.1002/wcms.1606**.

25 F. Neese, The SHARK integral generation and digestion system, *J. Comput. Chem.*, 2023, **44**(3), 381–396, DOI: **10.1002/jcc.26942**.

26 J. Tao, J. P. Perdew, V. N. Staroverov and G. E. Scuseria, Climbing the Density Functional Ladder: Nonempirical Meta-Generalized Gradient Approximation Designed for Molecules and Solids, *Phys. Rev. Lett.*, 2003, **91**(14), 146401.

27 F. Weigend and R. Ahlrichs, Balanced basis sets of split valence, triple zeta valence and quadruple zeta valence quality for H to Rn: Design and assessment of accuracy, *Phys. Chem. Chem. Phys.*, 2005, **7**(18), 3297–3305.

28 D. A. Pantazis and F. Neese, All-Electron Scalar Relativistic Basis Sets for the Lanthanides, *J. Chem. Theory Comput.*, 2009, **5**(9), 2229–2238, DOI: **10.1021/ct900090f**.

29 S. Grimme, J. Antony, S. Ehrlich and H. Krieg, A consistent and accurate ab initio parametrization of density functional dispersion correction (DFT-D) for the 94 elements H-Pu, *J. Chem. Phys.*, 2010, **132**(15), 154104, DOI: **10.1063/1.3382344**.

30 S. Grimme, S. Ehrlich and L. Goerigk, Effect of the damping function in dispersion corrected density functional theory, *J. Comput. Chem.*, 2011, **32**(7), 1456–1465, DOI: **10.1002/jcc.21759**.

31 F. Neese, An Improvement of the Resolution of the Identity Approximation for the Calculation of the Coulomb Matrix, *J. Comput. Chem.*, 2003, **24**, 1740–1747.

32 G. L. Stoychev, A. A. Auer and F. Neese, Automatic Generation of Auxiliary Basis Sets, *J. Chem. Theory Comput.*, 2017, **13**(2), 554–562, DOI: **10.1021/acs.jctc.6b01041**.

33 T. A. Beineke and J. Delgaudio, Crystal structure of ceric ammonium nitrate, *Inorg. Chem.*, 1968, **7**(4), 715–721, DOI: **10.1021/ic50062a020**.

34 G. B. Wijeratne, B. Corzine, V. W. Day and T. A. Jackson, Saturation Kinetics in Phenolic O–H Bond Oxidation by a Mononuclear Mn(III)–OH Complex Derived from Dioxygen, *Inorg. Chem.*, 2014, **53**(14), 7622–7634, DOI: **10.1021/ic500943k**.

35 D. B. Rice, S. D. Jones, J. T. Douglas and T. A. Jackson, NMR Studies of a MnIII-hydroxo Adduct Reveal an Equilibrium between MnIII-hydroxo and μ-Oxodimanganese(III,III) Species, *Inorg. Chem.*, 2018, **57**(13), 7825–7837, DOI: **10.1021/acs.inorgchem.8b00917**.

36 D. B. Rice, A. Munasinghe, E. N. Grotemeyer, A. D. Burr, V. W. Day and T. A. Jackson, Structure and Reactivity of (μ-Oxo)dimanganese(III,III) and Mononuclear Hydroxomanganese(III) Adducts Supported by Derivatives of an Amide-Containing Pentadentate Ligand, *Inorg. Chem.*, 2019, **58**(1), 622–636, DOI: **10.1021/acs.inorgchem.8b02794**.

37 D. F. Leto and T. A. Jackson, Mn K-Edge X-ray Absorption Studies of Oxo- and Hydroxo-manganese(IV) Complexes: Experimental and Theoretical Insights into Pre-Edge Properties, *Inorg. Chem.*, 2014, **53**(12), 6179–6194, DOI: **10.1021/ic5006902**.

38 S. Gupta, P. Arora, R. Kumar, A. Awasthi, B. Chandra, R. Eerlapally, J. Xiong, Y. Guo, L. Que Jr and A. Draksharapu, Formation of a Reactive [Mn(III)–O–Ce(IV)] Species and its Facile Equilibrium with Related Mn(IV)(OX) (X = Sc or H) Complexes, *Angew. Chem., Int. Ed.*, 2024, **63**(3), e202316378, DOI: **10.1002/anie.202316378**.

39 V. W. Manner, T. F. Markle, J. H. Freudenthal, J. P. Roth and J. M. Mayer, The first crystal structure of a monomeric phenoxyl radical: 2,4,6-tri-tert-butylphenoxyl radical, *Chem. Commun.*, 2008, (2), 256–258, DOI: **10.1039/B712872J**.

40 A. Draksharapu, W. Rasheed, J. E. M. N. Klein and L. Que Jr, Facile and Reversible Formation of Iron(III)–Oxo–Cerium (IV) Adducts from Nonheme Oxoiron(IV) Complexes and Cerium(III), *Angew. Chem., Int. Ed.*, 2017, **56**(31), 9091–9095, DOI: **10.1002/anie.201704322**.

41 M. Sankaralingam, Y.-M. Lee, D. G. Karmalkar, W. Nam and S. Fukuzumi, A Mononuclear Non-heme Manganese (III)–Aqua Complex as a New Active Oxidant in Hydrogen Atom Transfer Reactions, *J. Am. Chem. Soc.*, 2018, **140**(40), 12695–12699, DOI: **10.1021/jacs.8b07772**.

42 S. C. Sawant, X. Wu, J. Cho, K.-B. Cho, S. H. Kim, M. S. Seo, Y.-M. Lee, M. Kubo, T. Ogura, S. Shaik, *et al.*, Water as an Oxygen Source: Synthesis, Characterization, and Reactivity Studies of a Mononuclear Nonheme Manganese(IV) Oxo Complex, *Angew. Chem., Int. Ed.*, 2010, **49**(44), 8190–8194, DOI: **10.1002/anie.201000819**.

43 D. B. Rice, G. B. Wijeratne, A. D. Burr, J. D. Parham, V. W. Day and T. A. Jackson, Steric and Electronic Influence on Proton-Coupled Electron-Transfer Reactivity of a Mononuclear Mn(III)-Hydroxo Complex, *Inorg. Chem.*, 2016, **55**(16), 8110–8120, DOI: **10.1021/acs.inorgchem.6b01217**.

44 A. Murphy and T. D. P. Stack, Discovery and optimization of rapid manganese catalysts for the epoxidation of terminal olefins, *J. Mol. Catal. A: Chem.*, 2006, **251**, 78–88.

45 Y. Zang, J. Kim, Y. Dong, E. C. Wilkinson, E. H. Appelman and L. Que Jr., Models for Nonheme Iron Intermediates: Structural Basis for Tuning the Spin States of Fe(TPA) Complexes, *J. Am. Chem. Soc.*, 1997, **119**, 4197–4205.

46 Y.-M. Chiou and L. J. Que, Models for a-Keto Acid-Dependent Non-heme Iron Enzymes: Structures and Reactivity of [FeII(L)(O_2CCOPh)](ClO_4) Complexes, *J. Am. Chem. Soc.*, 1995, **117**, 3999–4013.

47 J. Kim, Y. Zang, M. Costas, G. R. Harrison, C. E. Wilkinson and L. Que Jr, A nonheme iron(II) complex that models the redox cycle of lipoxygenase, *J. Biol. Inorg. Chem.*, 2001, **6**(3), 275–284, DOI: **10.1007/s007750000198**.